FAST AND OPTIMAL DESIGN OF A K-BAND TRANSMIT-RECEIVE ACTIVE ANTENNA ARRAY

S. Yang, Q. Liu, J. Yuan, and S. Zhou

National Key Laboratory of Antennas and Microwave Technology
Xidian University
Xi'an 710071, China

Abstract—An active-antenna array with 18 transmit elements and 18 receive elements is designed and fabricated. This T/R array can work at two different frequencies (19.5 GHz and 21.5 GHz) with multiple levels of isolation between the transmit and receive channels. A hybrid element-level vector finite element and adaptive multilevel fast multipole method (ELVFEM/AMLFMA) is applied to simulation the performance parameters of the array element and the full array fast. To obtained the maximum directivity of the array, the best distances of the T/R elements in the array are optimized by using the genetic algorithm (GE) combining with VFEM/AMLFMA. The design efficiency of the array is improved at a ratio of 30%. Finally the performance of the T/R array fabricated is measured in experiments and some good results are obtained.

1. INTRODUCTION

Active-antenna array technology combines printed antennas and active devices with the goal of improving performance, increasing functionality, and reducing size relative to alternative architectures. Such arrays show potential for use in millimeter-wave commercial applications such as wireless local-area networks, electronic identification systems, and vehicle collision-avoidance radar.

The fundamental goal of the work of this paper is to achieve full-duplex operation by using two different frequencies (19.5 GHz and 21.5 GHz) with multiple levels of isolation between the transmit and receive channels. The primary application for this full-duplex transmit-receive active-antenna array is its use as a front end to a communications system. Fed in the near field at the focal point, the array is designed to radiate directly into space. Reciprocally, incoming

signals are received from free space, amplified, and focused onto a receiver at the focal point.

2. SIMULATION METHOD

To analysis plane micro-stripe antenna array like shown in Figure 1, hybrid finite element and multilevel fast multipole method (FEM/MLFMA) can be applied. The field in the region of dielectric substrate can be formulated into an equivalent problem with the function

$$F(\boldsymbol{E}) = \frac{1}{2} \int_V \left[\frac{1}{\mu_r} (\nabla \times \boldsymbol{E}) \cdot (\nabla \times \boldsymbol{E}) - k_0^2 \varepsilon_r \boldsymbol{E} \cdot \boldsymbol{E} \right] dV$$
$$+ jk_0 \int_{S_e} (\boldsymbol{E} \times \boldsymbol{H}) \cdot \hat{n} dS \tag{1}$$

where

V interior volume of the substrate;
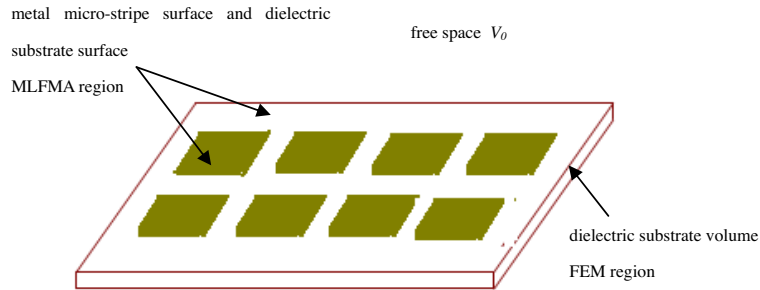
S_e outside surface of the antenna;

$\hat{n}$ outward unit normal to antenna surface;

k_0 free-space wave number;

On the antenna surface S_e, a group of combined field integral equation (CFIE) can be employed for both the micro-stripe and substrate surface.

$$\alpha \cdot \text{EFIE} + (1 - \alpha) \cdot \text{MFIE} \quad (0.2 \leq \alpha \leq 1) \tag{2}$$

In Equation (2), EFIE is the electric field integral equation and MFIE is the magnetic field integral equation. Let's assume that the antenna

metal micro-stripe surface and dielectric
substrate surface
MLFMA region
free space V_0
dielectric substrate volume
FEM region

Figure 1. A micro-stripe antenna array model and the corresponding solving region for FEM and MLFMA.

is combined of $M - 1$ metal parts and a dielectric substrate part, and the region they occupied is $V_l(l = 1 \ldots M)$. The region V_0 out of the antenna is defined as free space. $M + 1$ equations should be needed for the problem we discussed.

On the boundary of V_0 region EFIE yields

$$\boldsymbol{E}^s(\boldsymbol{r}) = -jk_0\eta \int_{S_0} \boldsymbol{J}_0(\boldsymbol{r}')\overline{\overline{G}}(\boldsymbol{r}, \boldsymbol{r}')dr' - \nabla \times \int_{S_0} \boldsymbol{M}_0(\boldsymbol{r}')G(\boldsymbol{r}, \boldsymbol{r}')dr'$$
(3)

MFIE yields

$$\boldsymbol{H}^s(r) = -j\frac{k_0}{\eta} \int_{S_0} \boldsymbol{M}_0(\boldsymbol{r}')\overline{\overline{G}}(\boldsymbol{r}, \boldsymbol{r}')dr' + \nabla \times \int_{S_0} \boldsymbol{J}_0(\boldsymbol{r}')G(\boldsymbol{r}, \boldsymbol{r}')dr'$$
(4)

where $\boldsymbol{J} = \hat{n} \times \boldsymbol{H}$ and $\boldsymbol{M} = \boldsymbol{E} \times \hat{n}$, $\boldsymbol{J}$ denotes the electric current on boundary surface and $\boldsymbol{M}$ denotes magnetic current on boundary surface. $G(\boldsymbol{r}, \boldsymbol{r}')$ and $\overline{\overline{G}}(\boldsymbol{r}, \boldsymbol{r}')$ are the Green's function and dyadic Green's function in free space.

On the boundary of V_i region, EFIE yields

$$0 = -jk\eta \int_{S_l} \boldsymbol{J}_l(\boldsymbol{r}')\overline{\overline{G}}(\boldsymbol{r}, \boldsymbol{r}')dr' - \nabla \times \int_{S_l} \boldsymbol{M}_l(\boldsymbol{r}')G(\boldsymbol{r}, \boldsymbol{r}')dr' \quad (5)$$
$$(\boldsymbol{M} = 0 \text{ for the metal surface})$$

MFIE yields

$$0 = -j\frac{k}{\eta} \int_{S_l} \boldsymbol{M}_l(\boldsymbol{r}')\overline{\overline{G}}(\boldsymbol{r}, \boldsymbol{r}')dr' + \nabla \times \int_{S_l} \boldsymbol{J}_l(\boldsymbol{r}')G(\boldsymbol{r}, \boldsymbol{r}')dr' \quad (6)$$

Combing Equations (1), (3)–(6) and using vector edge basis function, we can obtain the matrix equation of complete system

$$\begin{bmatrix} \boldsymbol{K}_{II} & \boldsymbol{K}_{IS} & 0 \\ \boldsymbol{K}_{SI} & \boldsymbol{K}_{SS} & \boldsymbol{B} \\ 0 & \boldsymbol{P}_1 & \boldsymbol{Q}_1 \\ . & . & . \\ 0 & \boldsymbol{P}_M & \boldsymbol{Q}_M \\ 0 & \boldsymbol{P}_0 & \boldsymbol{Q}_0 \end{bmatrix} \begin{Bmatrix} \boldsymbol{E}_I \\ \boldsymbol{E}_S \\ \boldsymbol{H}_{1S} \\ . \\ \boldsymbol{H}_{MS} \\ \boldsymbol{H}_{0S} \end{Bmatrix} = \begin{Bmatrix} 0 \\ 0 \\ \boldsymbol{b}_1 \\ . \\ \boldsymbol{b}_{MS} \\ \boldsymbol{b}_0 \end{Bmatrix}$$
(7)

In Equation (7), $\{\boldsymbol{E}_I\}$ is a vector containing the discretized electric field inside V, $\{\boldsymbol{E}_S\}$ and $\{\boldsymbol{H}_S\}$ are the vectors containing the discretized electric and magnetic fields on S_e. Furthermore,

$[\boldsymbol{K}_{II}]$, $[\boldsymbol{K}_{IS}]$, $[\boldsymbol{K}_{SI}]$, $[\boldsymbol{K}_{SS}]$, and $[\boldsymbol{B}]$ are sparse submatrices and, in particular, $[\boldsymbol{K}_{II}]$ and $[\boldsymbol{K}_{SS}]$ are symmetric, $[\boldsymbol{B}]$ is skew symmetric and $[\boldsymbol{K}_{IS}] = [\boldsymbol{K}_{SI}]^T$, where the superscript T denotes a transpose operation. $[\boldsymbol{P}]$ and $[\boldsymbol{Q}]$ are the dense submatrices of discretized CFIE which is employed on S_e.

To improve the performance of FEM, the multiply of $[\boldsymbol{K}]$ and vector can be change into the multiply of a series of small scale matrices and vector. The $[\boldsymbol{K}]$ yields

$$\boldsymbol{K} = \sum_{i=1}^{N} \boldsymbol{K}_i \tag{8}$$

where $[\boldsymbol{K}_i]$ is the global coefficient matrix of ith volume tetrahedral element in $[\boldsymbol{K}]$ and N is the total number of tetrahedral elements. In matrix $[\boldsymbol{K}_i]$ the matrix elements on the rows and columns related to ith volume tetrahedral element of region V are not equal to zero, these elements are also the elements in the coefficient matrix of ith volume tetrahedral element. Thus, the multiply of $[\boldsymbol{K}]$ and unknown vector yields

$$\boldsymbol{b} = \boldsymbol{K}\boldsymbol{x} = \left(\sum_i \boldsymbol{K}_i \boldsymbol{x}\right) = \sum_i (\boldsymbol{K}_i \boldsymbol{x}) = \sum_i (\boldsymbol{K}_i \boldsymbol{x}_i) = \sum_i \boldsymbol{b}_i \tag{9}$$

where

$$\boldsymbol{b} = \{0, 0, \boldsymbol{b}\}^T, \quad \boldsymbol{x} = \{\boldsymbol{E}_I, \boldsymbol{E}_S, \boldsymbol{E}_s\}^T$$

In Equation (9), $\{x_i\}$ is the vector corresponding to $[\boldsymbol{K}_i]$, the nonzero elements in $\{x_i\}$ are the elements in $\{x\}$. The multiply of $[\boldsymbol{K}_i]$ and $\{x_i\}$ is determined by ith volume tetrahedral element only and $[\boldsymbol{K}_i]\{x_i\} = [\boldsymbol{K}^i]\{x^i\}$, where $[\boldsymbol{K}^i]$ is the small scale dense coefficient matrix of ith volume tetrahedral element and $\{x^i\}$ is the corresponding unknown vector of $[\boldsymbol{K}^i]$. The multiply of global coefficient matrix $[\boldsymbol{K}]$ and unknown vector $\{\boldsymbol{E}_I, \boldsymbol{E}_S, \boldsymbol{H}_S\}^T$ can be calculated at element-level. Because the multiply calculation of zero elements in $[\boldsymbol{K}_i]$ and corresponding elements in $\{x_i\}$ can be omitted and all the computation is finished at element-level, the CPU time and memory requirement of FEM can be reduced significantly and this method can be called as element-level vector finite element method(ELVFEM).

In Equation (7), each linear matrix equation of V_l surface can be written as

$$\sum_{i=1}^{N_s} \boldsymbol{P}_{ji}\boldsymbol{e}_{si} + \sum_{i=1}^{N_s} \boldsymbol{Q}_{ji}\boldsymbol{h}_{si} = \boldsymbol{b}_j \tag{10}$$

when MLFMA is applied. Where

$$
\sum_{i=1}^{N_s} \boldsymbol{P}_{ji} \boldsymbol{e}_{si} = \sum_{i \notin G_{m'}} \boldsymbol{P}_{ji} \boldsymbol{e}_{si} + \oint_s d^2 \widehat{k} \boldsymbol{V}_{fmj}^P \left(\widehat{k} \right)
$$
$$
\cdot \sum_{m' \in G_{m'}} T_L \left(\widehat{k} \cdot \widehat{r}_{mm'} \right) \sum_{i \in G_{m'}} \boldsymbol{V}_{sm'i} \left(\widehat{k} \right) \boldsymbol{e}_{si} \qquad (11)
$$

$$
\sum_{i=1}^{N_s} \boldsymbol{Q}_{ji} \boldsymbol{h}_{si} = \sum_{i \notin G_{m'}} \boldsymbol{Q}_{ji} \boldsymbol{h}_{si} + \oint_s d^2 \widehat{k} \boldsymbol{V}_{fmj}^Q \left(\widehat{k} \right)
$$
$$
\cdot \sum_{m' \in G_{m'}} T_L \left(\widehat{k} \cdot \widehat{r}_{mm'} \right) \sum_{i \in G_{m'}} \boldsymbol{V}_{sm'i} \left(\widehat{k} \right) \boldsymbol{h}_{si} \qquad (12)
$$
$$
e_{si} \in \{\boldsymbol{E}_S\}, h_{si} \in \{\boldsymbol{H}_S\}
$$

N_s is the number of surface triangle elements, $\boldsymbol{V}_{sm'i}$, T_L and $\boldsymbol{V}_{fmj}$ are aggregation operator, translation operator and disaggregation operator. While using the advanced MLFMA method called adaptive multilevel fast multipole algorithm (AMLFMA) [1], formulation (11) and (12) can be written as

$$
\sum_{i=1}^{N_s} Z_{ji} I_i = \sum_{i \notin G_{m'}} Z_{ji} I_i + \oint_s d^2 \widehat{k} \boldsymbol{V}_{fmj}^{SPD} \left(\widehat{k} \right) \cdot \sum_{m' \in G_{m'}} FFT^{-1} \Big\{ FFT \Big[T_L \left(\widehat{k} \cdot \widehat{r}_{mm'} \right) \Big]
$$
$$
\times FFT \left[\sum_{i \in G_{m'}} \boldsymbol{V}_{sm'i}^{*SPD} \left(\widehat{k} \right) I_i \right] \Big\} + \boldsymbol{V}_{fmj}^{SPD} \left(\widehat{k}_0 \right)
$$
$$
\cdot \sum_{m' \in SFG_{m'}} FFT^{-1} \Big\{ FFT \Big[T_L^{far} \Big] \times FFT \left[\sum_{i \in SFG_{m'}} \boldsymbol{V}_{sm'i}^{*SPD} \left(\widehat{k}_0 \right) I_i \right] \Big\} \quad (13)
$$

In AMLFMA the fast Fourier transformation (FFT) is used to calculate the translation process of MLFMA and higher performance can be obtained.

The computational complexity of the ELVFEM/AMLFMA method introduced above is only about $0.7 \times O(N_v + N_s \lg N_s)$ and is memory requirement is $0.7 \times O(N_v + N_s)$, where N_v denotes the number of volume unknowns of FEM region and N_s denotes the number of surface unknowns.

3. ANTENNA DESIGN

3.1. Element Design

The T/R array is comprised of three layers of dielectric [2, 18]. The primary layer is Rogers TMM10i, the middle layer is Rohm Rohacell 31 HF, and the last layer is Sheldahl Novaclad G2300. The substrate which supports the majority of the microwave circuitry is Rogers TMM10i with a thickness of 381 μm, a relative permittivity of $\varepsilon_r = 9.806$, a loss tangent of $\tan \delta = 0.002$, and a metal thickness of 17.5 μm. To prevent loss in the form of surface waves, the substrate was chosen to be thin ($\lambda_d = 13$) relative to the dielectric wavelength [2]. Substrate values are summarized in Table 1.

Table 1. Array substrate parameters shown in order of assembly.

Product	Material	ε_r	$\tan \delta$	Thickness $h(\mu m)$
Rogers TMM10i	Metal	1.0	-	17.5
	Substrate	9.8	0.002	380
	Metal	1.0	-	17.5
Rohm Rohacell 31HF	Foam	1.07	0.004	1000
Sheldahl Novaclad G2300	Metal	1.0	-	17.5
	Polyimide	3.3	0.011	50.8

Standard and slot-fed patches are the fundamental building blocks of the array. The slot-fed patch simultaneously increases aperture efficiency and provides a coupling path through the array. The standard patch on the high permittivity substrate is small enough to be integrated into the complex front side circuitry while still providing reduced coupling relative to other antennas.

Coplanar waveguide (CPW) is utilized because planar fabrication is required. In practice, the two CPW ground electrodes are limited in width in order to suppress leaky parallel-plate modes. These unwanted modes would otherwise be supported between the side grounds and the substrate ground. This type of transmission line is known as finite-width ground-backed coplanar waveguide (FW-GBCPW) [3]. The T/R array makes use of a combination of FW-GBCPW and micro-stripe transmission lines (MSL).

The MSL provides connectivity to the standard patch antennas and slot couplers, and the CPW provides transitions to and from the MMIC. The benefit of using a hybrid CPW-MSL design as opposed to a simpler all-MSL design is the reduction of fabrication complexity by the elimination. The final dimensions for the transmission lines are summarized in Table 2.

Table 2. Transmission-line specifications.

CPW Dimensions		MSL Dimensions		Substrate Values	
W_{cpw}	290 µm	W_{ms}	360 µm	ε_r	9.8
S_{cpw}	245 µm	λ_{ms}	6.0 mm	$\tan\delta$	0.002
B_{cpw}	780 µm			h	380
λ_{cpw}	6.5 µm			t	17.5

Probe-station measurements require that the input and output port (even in the case of a radiator) are on the same side of the substrate and that probed ports terminate in a CPW transmission line. This necessitates the use of multiple transitions to measure the various unit-cell components. The design of novel testing circuitry, as well as unit-cell components used in the final implementation of the array are presented in Figure 2.

Table 3. Dimensions of the slot coupler and antennas.

Coupler Dimensions		Slot Dimensions		Slot-Fed Patch Dimensions	
L_{sc}	3.55 mm	L_{sa}	4.65 mm	L_{p}	6.55 mm
W_{sc}	0.35 mm	W_{sa}	1.20 mm	W_{p}	5.90 mm

The slot coupler is comprised of two CPW-to-MSL transitions aligned on opposite sides of a slot in a shared substrate ground plane. The transition from CPW to MSL occurs in three coupled micro-stripe transmission lines.

The high front-to-back ratio for input-output isolation is the primary reason for using the slot-fed patch antenna, the increase in gain provided by the thick, low-permittivity substrate significantly improves the aperture efficiency of the array. The large slot-fed patch also has a larger bandwidth. This design also achieves high isolation between feed and non-feed sides.
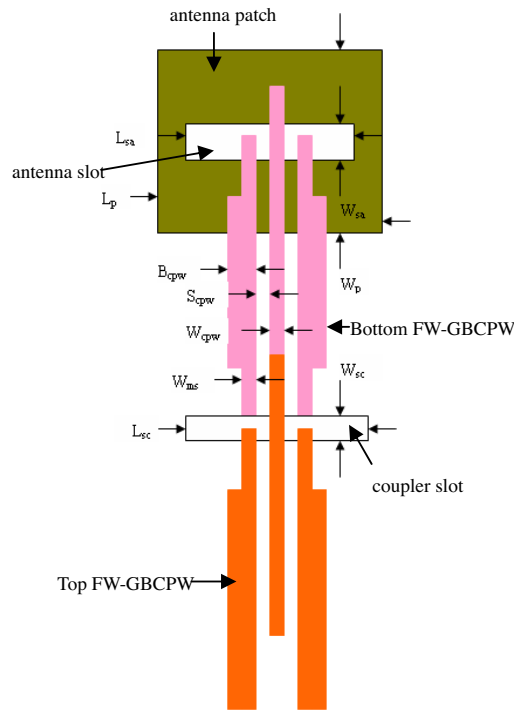
Figure 2. Balanced coupler and patch antenna with characteristic geometric parameters labeled. K-band ground-backed CPW balanced coupler with the transition-fed patch antenna.

3.2. Element and Channel Coupling

Amplification is performed in transmission (19.5 GHz) by an HPHMMC-5620 single-bias power amplifier (PA) with a maximum small-signal gain of 17 dB from 6 to 20 GHz (Figure 3(a)). Amplification is performed in reception (21.5 GHz) by an Alpha AA022N1-00 single-bias low noise amplifier (LNA) with a maximum small-signal gain of 22 dB from 20 to 24 GHz and a noise figure of 2.5 dB (Figure 3(b)).

Simulated channel coupling by using ELVFEM/AMLFMA is shown in Table 4. The excitation of ELVFEM/AMLFMA is selected as voltage source and these sources are set on the positions of the active PA and LNA. Isolation between channels is provided by the use of band-pass components such as frequency dependent transitions, couplers, and antennas. Additional isolation is furnished by the orthogonal polarization between the unit cells of opposite channels.

   The reduction of the coupling from input to output antenna is achieved by the use of orthogonal polarizations for the input and output antennas, and by a ground plane, which separates the input and output antennas. Thus, the only antennas which are copolarized are antennas of the other channel on the opposite side of the ground plane.

(a)　　　　　　　　　　(b)
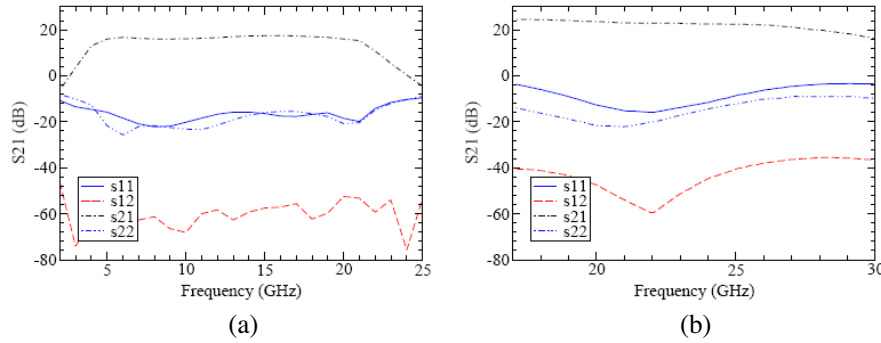
Figure 3. Power amplifier (a) and low-noise amplifier (b) specifications. The power amplifier amplifies the outgoing 19.5 GHz channel. The low-noise amplifier amplifies the incoming 21.5 GHz channel.

Table 4. Simulated coupling between channels in the passive array.

| Coupling Path	Side	Freq (GHz)	Coupling (dB)
$PA_{19.5} \rightarrow LNA_{19.5}$	Non-feed	19.5	-52
$PA_{21.5} \rightarrow LNA_{21.5}$	Non-feed	21.5	-45
$LNA_{19.5} \rightarrow PA_{19.5}$	feed	19.5	-31
$LNA_{21.5} \rightarrow PA_{21.5}$	feed	21.5	-23

3.3. Unit-cell Design

A single full-duplex transmit-receive unit cell is comprised of two independent orthogonal unit cells, one for each channel (Figure 4 and Figure 5). A single channel's unit cell contains a patch antenna, a coplanar waveguide section with amplifier, and a slot-fed patch antenna. A unit cell dimension measures $8.0 \times 16.0 \, \text{mm}^2$.

   The full-duplex transmit-receive array is designed using planar multilayer processing eliminating vias and air bridges. This is achieved by integrating micro-stripe line (MSL) and finite-width ground-backed
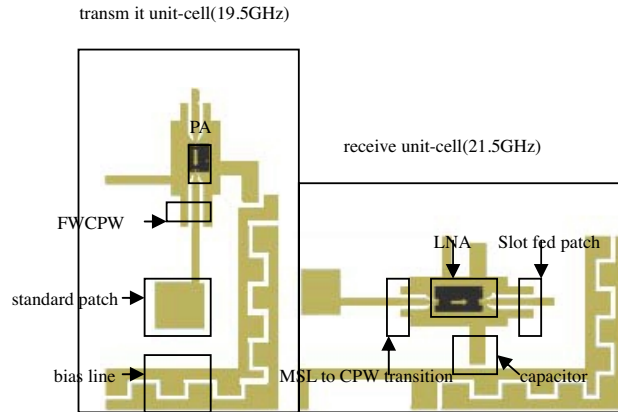
Figure 4. The 19.5 GHz transmit (left) and 21.5 GHz receive (right) unit cells with important features labeled.
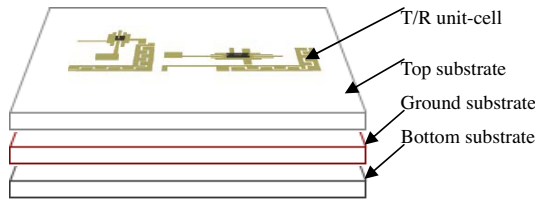
Figure 5. Assembly drawing of the transmit and receive unit cells.

coplanar waveguide (fCPW) within a single unit cell. The MSL provides the connection to the standard patch antenna on the feed side of the array; the fCPW provides a transition to the MMIC, which eliminates the need for vias required with MSL. Transitions between MSL and fCPW occurs in a section of three coupled micro-stripe transmission lines of length $\lambda_{ms}/4$ at the unit-cell's frequency of operation.

This transition feeds the slot-fed patch antenna on rigid foam through a slot in the ground plane on the opposite side of the MMIC. The integrated slot-transition feed reduces space consumption and improves the front-to-back ratio (36 dB) of the slot-fed patch relative to a standard MSL feed. Additionally, the slot-fed patch antenna is polarized orthogonally to the Micro-stripe-fed patch antenna eliminating the need for a 90° bend in the unit-cell line. The number of air bridges is minimized by keeping the transmission lines straight.

The aperture efficiencies of the unit cells are summarized by using ELVFEM/AMLFMA in Table 5. The aperture efficiencies are calculated with Equation (14) using the area of two unit cells as A_{phys}. It should be noted that the aperture efficiency of the array is most strongly influenced by the array's overall array factor rather than by the individual unit cell, but is included here to highlight the relative directivities of the antennas.

Aperture efficiency is the ratio of the effective area of a spatial power combiner to the physical area.

$$\eta_\alpha = \frac{A_{\text{eff}}}{A_{\text{phys}}} \tag{14}$$

The effective area of a spatial power combiner is proportional to the directive gain

$$A_{\text{eff}} = \frac{\lambda^2}{4\pi} G \tag{15}$$

which is related to directivity by

$$G = \eta_r D \tag{16}$$

where η_r is the system efficiency which includes substrate losses, ohmic losses, and polarization and impedance mismatches.

**Table 5.** Antenna aperture-efficiency calculations.

	Transmit channel (19.5 GHz)	Receive channel (21.5 GHz)
A_{eff}	$160.3 \times 10^{-6}\,\text{m}^2$	$135.2 \times 10^{-6}\,\text{m}^2$
A_{phys}	$295.6 \times 10^{-6}\,\text{m}^2$	$296.5 \times 10^{-6}\,\text{m}^2$
η_a	$54.2\%\ (-2.65\,\text{dB})$	$45.6\%\ (-3.41\,\text{dB})$

Because the slot-coupler transition is used to feed the slot-fed patch antenna, it is the first circuit characterized. The simulated return loss by using ELVFEM/AMLFMA of the coupler is less than 10 dB over a 12% bandwidth from 17 GHz to 20 GHz with a 2 dB average insertion loss over the pass band (Figure 6).

3.4. Array Layout Design and Optimization [4–12, 14, 20, 21]

There are 18 transmitting and 18 receiving unit cells will be arranged in alternating diagonal rows (Figure 7). To obtained the optimization

distances of elements in the array, genetic algorithm is used to optimize the array layout to obtained both the maximum directivity of transmit array and receive array [5–7].

(a)   (b)
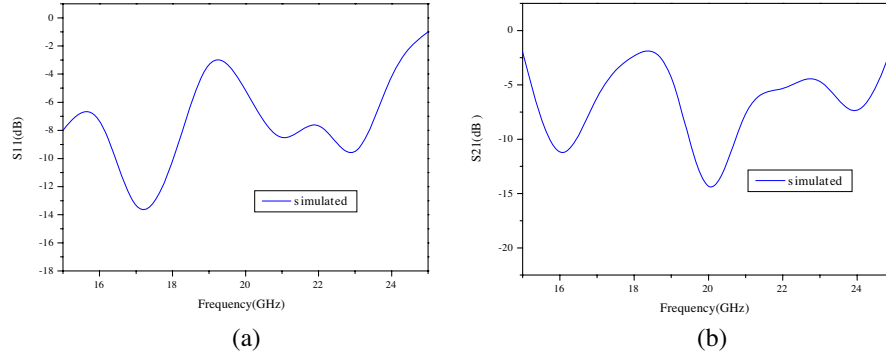
Figure 6. Simulated reflection (a) and transmission (b) coefficients of the slot coupler.
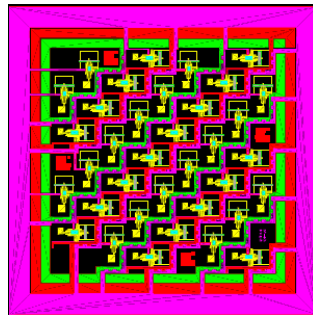
Figure 7. The CAD model of K-band full-duplex transmit-receive active-antenna array shown from the feed side.

Defined the directivity of a planner array include $N \times N$ elements as

$$D = \frac{4\pi}{\int_0^{2\pi} \int_0^{\pi} |F(\theta, \phi)|^2 \sin\theta d\theta d\phi} \tag{17}$$

where

$$F(\theta, \phi) = 4\cos\theta \left\{ \sum_{m=1}^{N_x} I_{xm} \cos\left[k\left(\sum_{i=1}^{m} d_{xi} - \frac{1}{2}d_{x1} \right) \sin\theta\cos\phi \right] \right\}$$

$$\times \left\{ \sum_{n=1}^{N_y} I_{yn} \cos\left[k\left(\sum_{j=1}^{n} d_{yj} - \frac{1}{2}d_{y1} \right) \sin\theta\sin\phi \right] \right\} \quad (18)$$

to obtained the best directivity, the current $I_{mn}(I_{mn} = I_{xm}I_{yn})$, distances d_{xi} and d_{yj} in x direction and y direction should be selected as the variables to be optimized.

For the array include both T/R channels, the target function and the fitness function can be selected as

$$f = \max\left(\alpha_1 D_T + \alpha_2 D_R\right)$$

$$= \min\left(-\alpha_1 \frac{4\pi}{\int_0^{2\pi}\int_0^{\pi} |F_T(\theta,\phi)|^2 \sin\theta d\theta d\phi} \right.$$

$$\left. -\alpha_2 \frac{4\pi}{\int_0^{2\pi}\int_0^{\pi} |F_R(\theta,\phi)|^2 \sin\theta d\theta d\phi} \right) \quad (19)$$

$$(0 < \alpha_1 < 1,\ 0 < \alpha_2 < 1,\ \alpha_1 + \alpha_2 = 1)$$

$$\text{fitness} = \alpha_1 D_T + \alpha_2 D_R \quad (20)$$

where D_T and D_R are the directivities of the transmit array and receive array, a_1 and a_2 are the weight coefficients. The currents and the distances in the two directions of both the transmit array and receive array are the variables to be optimized.

In the process of optimization, to compute the fitness function precisely and fast(computing the current distribution will consumed a lot time), the parallel ELVFEM/AMLFMA [1] is used via a cluster of personal computers which includes 20 computers with Intel PIV 2.0 GHz processor and 1 GB memory. While simulating, the CAD model (Figure 7) of the T/R array is discrete and there are total 152738 unknowns for parallel ELVFEM/AMLFMA to solve. The parallel ELVFEM/AMLFMA is called for 150 times in the optimization process and each time consumed 1.6 hours (368 MB memory is consumed by each computer). The total optimization process consumed about 10 days. If the traditional parallel FEM/MLFMA is used, at least 15 days will be consumed to finish the whole optimization process on the same

cluster. The optimization efficiency is improved at a ratio about 30%. The main flow chart of the optimization process is shown in Figure 8.

The optimized distance between neighboring antennas for a given frequency is 12×24 mm. This spacing generates grating lobes at $36°$ and $35°$ at 19.5 GHz and 21.5 GHz in the diagonal plane corresponding
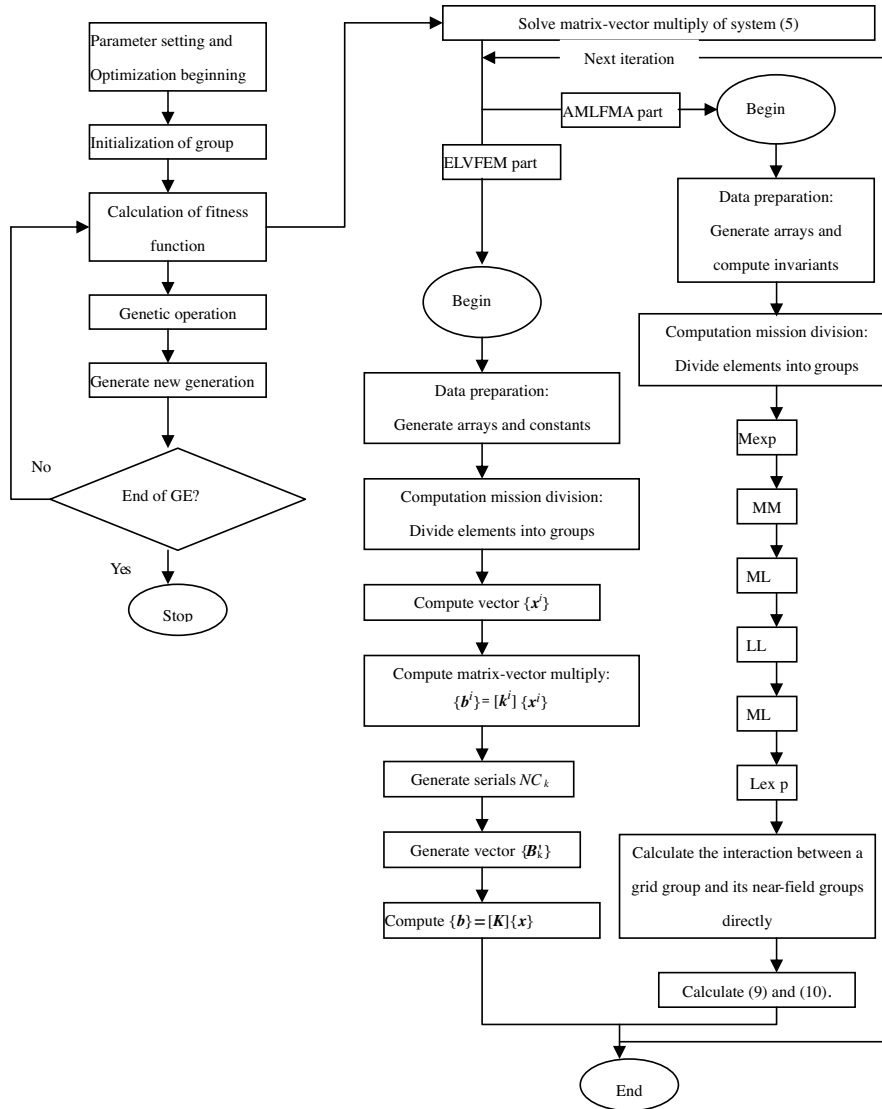


Figure 8. Main flow chart of the optimization process.

to the largest row separation. Equivalently, a single transmitter in the far field generates three maxima on the focal plane with similar angular separation.

Simulated far field E-plane and H-plane at 19.5 GHz (a) and 21.5 GHz (b) of the optimized array by using ELVFEM/AMLFMA is shown in Figure 9. The CPU time consumed by ELVFEM/AMLFMA is 187961 seconds and the memory consumed is 6171MB (152738 unknowns). All the simulation work is finished on a workstation with Intel PIV 2.0 GHz processor and 10 GB memory.

4. MEASUREMENT AND ANALYSIS [13, 15–17, 19]

4.1. Far-field Patterns

The fabricated T/R antenna array is shown in Figure 10 and its far-field patterns are taken at 19.5 GHz in transmission and at 21.5 GHz in reception. Figure 11 shows the measured active patterns for the PA in transmission at 19.5 GHz and the LNA in reception at 21.5 GHz. The experiment results have a good agreement with the simulation results (Figure 9).


(a)   (b)
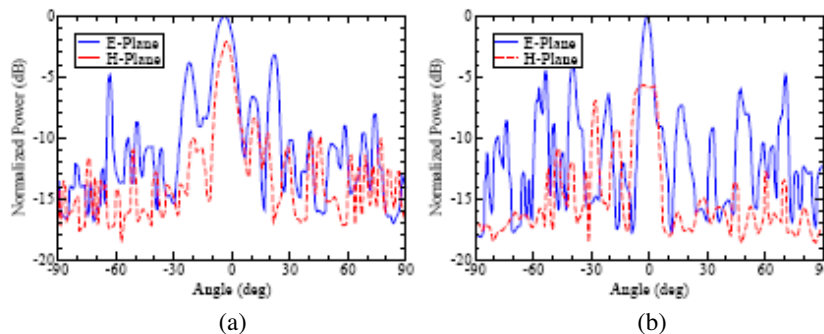
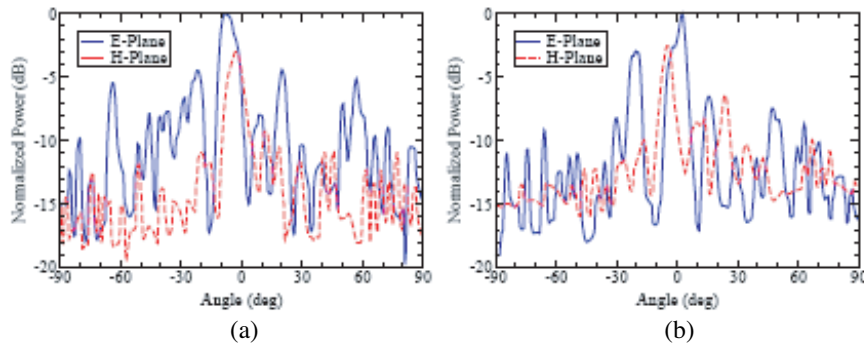**Figure 9.** Simulated far field E-plane and H-plane at 19.5 GHz (a) and 21.5 GHz (b).

4.2. Small-signal Gain

Small-signal measurements are performed with an HP 8510C vector network analyzer and are normalized to a free-space calibration performed through an array-sized aperture.

Active small-signal full-duplex measurements are presented in Figure 12. Both channels are stable with little or no effect on the
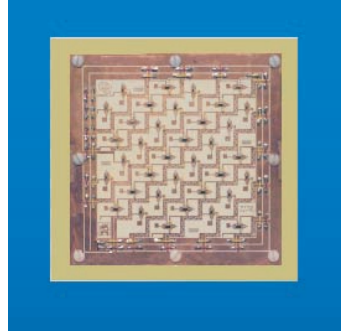
Figure 10. The fabricated T/R antenna array.

(a)   (b)

Figure 11. Measured far-field E-plane and H-plane for the PA at 19.5 GHz (a) and LNA at 21.5 GHz (b).

performance of the other channel. The transmit array channel provides -10.0 dB of gain at 19.0 GHz which is 3.0 dB above the passive array at 3.55 V and 1.73 A. The receive channel provides -3.8 dB of gain at 21.0 GHz with a 7.5 dB gain above the passive array at 4.00 V and 0.84 A. The presence or absence of bias to one channel has no effect on the gain of the opposing channel within the error of measurement.

Note that the difference in gain between the transmit and receive channel at the receive channel's frequency of operation is separated by 25 dB. This isolation is critical to prevent the transmit channel from amplifying noise at the operation frequency of LNA.

The maximum gain of the MMIC are limited by oscillations. The bias levels at which oscillations occur in one MMIC are unaffected by the bias level or state of the other MMIC. Evidence supports that the oscillations occur at the devices themselves and are most likely due

to an impedance mismatch presented to the amplifier by wire bond inductance or the wire bond-transmission interface.

4.3. Saturated Power

Figure 13 shows the measured power at the output of the array as a function of the power present at the face of the array. Limitations imposed by MMIC instability prevent the acquisition of the maximum operating power. Maximum power out is measured to be 6 mW.
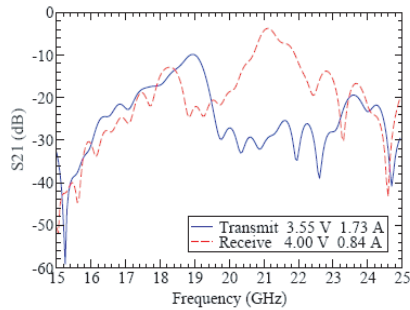
Figure 12. Measurement of the active array operating in full-duplex showing transmission response through the array as a function of frequency.
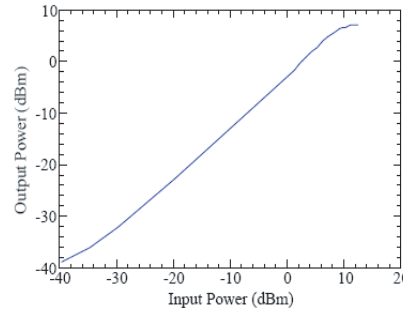
Figure 13. Output power at the face of the array versus input power at the face of the array.

5. CONCLUSION

In this paper, an active T/R antenna array work at different frequency is designed and fabricated. Because the array is electrically large at its work frequency, to design it efficiently a ELVFEM/AMLFMA method is applied to accomplish the simulation work and the GE algorithm is also used to optimize the array layout. Finally the array is fabricated according to the simulation results and the optimization results.

By experimenting on the fabricated array we can see that the primary goal of demonstrating the first spatial power combiner to provide full-duplex transmit-receive functionality and preventing inter-channel coupling both have been met.

REFERENCES

1. Yuan, J., Q.-Z. Liu, and J.-L. Guo, "Fast parallel algorithm for electromagnetic scattering problem via vector-FEM/MLFMA method," *Acta Electronica Sinica*, Vol. 36, No. 3, 520–526, 2008.

2. Vandelay, A., M. Von Nostrand, and K. Varnsen, "Signed-field analysis of surface mode losses," *IEEE Microwave and Guided Wave Letters*, 1989.

3. Shih, Y. C. and T. Itoh, "Analysis of conductor-backed coplanar waveguide," *Electronics Letters*, Vol. 18, 538–540, June 1982.

4. Kumar, B. P. and G. R. Branner, "Design of unequally spaced arrays for performance improvement," *IEEE Trans. Antennas Propagat.*, Vol. 47, No. 3, 511–523, 1999.

5. Yan, K.-K. and Y. Lu, "Side-lobe reduction in array pattern synthesis using genetic algorithm," *IEEE Trans. Antennas Propagat.*, Vol. 45, No. 7, 1117–1122, 1997.

6. Weile, D. S. and E. Michielssen, "Genetic algorithm optimization applied to electromagnetics: A review," *IEEE Trans. Antennas Propagat.*, Vol. 45, No. 3, 343–353, 1997.

7. Haupt, R. L., "An introduction to genetic algorithm for electromagnetics," *IEEE Antennas Propagat. Mag.*, Vol. 37, No. 2, 7–15, 1995.

8. Yuan, J., Y. Qiu, J. Guo, Y. Zou, and Q.-Z. Liu, "Fast analysis of antenna mounted on electrically large composite objects," *Progress In Electromagnetics Research*, PIER 80, 29–44, 2008.

9. Guo, J. L., J. Y. Li, and Q. Z. Liu, "Electromagnetic analysis of coupled conducting and dielectric targets using mom with a pre-conditioner," *Journal of Electromagnetic Waves and Applications*, Vol. 19, No. 9, 1223–1236, 2005.

10. Guo, J. L., J. Y. Li, and Q. Z. Liu, "Analysis of antenna array with arbitrarily shaped radomes using fast algorithm based on VSIE," *Journal of Electromagnetic Waves and Applications*, Vol. 20, No. 10, 1399–1410, 2006.

11. Qiu, Y., J. Yuan, J. Tian, and Y.-J. Xie, "Antenna position optimal design for reducing interference," *2004 International Symposium on EMC Proceedings*, 689–693, June 2004.

12. Hassani, H. R. and M. Jahanbakht, "Method of moment analysis of finite phased array of aperture coupled circular microstrip patch antennas," *Progress In Electromagnetics Research B*, Vol. 4, 197–210, 2008.

13. Xiao, S.-Q., J. Chen, X.-F. Liu, and B.-Z. Wang, "Spatial focusing characteristics of time reversal UWB pulse transmission with different antenna arrays," *Progress In Electromagnetics Research B*, Vol. 2, 223–232, 2008.

14. Rocca, P., L. Manica, and A. Massa, "An effective excitation matching method for the synthesis of optimal compromises between sum and difference patterns in planar arrays," *Progress In Electromagnetics Research B*, Vol. 3, 115–130, 2008.

15. Naghshvarian-Jahromi, M., "Novel Ku band fan beam reflector back array antenna," *Progress In Electromagnetics Research Letters*, Vol. 3, 95–103, 2008.

16. Yuan, H.-W., S.-X. Gong, P.-F. Zhang, and X. Wang, "Wide scanning phased array antenna using printed dipole antennas with parasitic element," *Progress In Electromagnetics Research Letters*, Vol. 2, 187–193, 2008.

17. Abdelaziz, A. A., "Improving the performance of an antenna array by using radar absorbing cover," *Progress In Electromagnetics Research Letters*, Vol. 1, 129–138, 2008.

18. Cui, B., J. Zhang, and X.-W. Sun, "Single layer microstrip antenna arrays applied in millimeter-wave radar front-end," *J. of Electromagn. Waves and Appl.*, Vol. 22, No. 1, 3–15, 2008.

19. He, Q.-Q., Q. Wang, and B.-Z. Wang, "Conformal array based on pattern reconfigurable antenna and its artificial neural model," *J. of Electromagn. Waves and Appl.*, Vol. 22, No. 1, 99–110, 2008.

20. Zhai, Y.-W., X.-W. Shi, and Y.-J. Zhao, "Optimized design of ideal and actual transformer based on improved micro-genetic algorithm," *J. of Electromagn. Waves and Appl.*, Vol. 21, No. 13, 1761–1771, 2007.

21. Rocca, P., L. Manica, and A. Massa, "An effective excitation matching method for the synthesis of optimal compromises between sum and difference patterns in planar arrays," *Progress In Electromagnetics Research B*, Vol. 3, 115–130, 2008.